

Efficient and dynamic neural geometry of value and modality encoding in the primate putamen for value-guided behavior

Received: 28 November 2024

Seong-Hwan Hwang^{1,2,4}, Ji-Woo Lee^{1,4}, Sung-Phil Kim³ & Hyoung F. Kim^{1,2} 

Accepted: 28 August 2025

Published online: 17 September 2025

 Check for updates

The basal ganglia process diverse reward values from various modalities using limited resources, necessitating efficient processing. The convergence of sensory reward values at the single-neuron level enables the efficient use of limited neural resources. However, this raises a critical question: does such convergence compromise modality-specific information and degrade the overall information quality? Here, we reveal that the population representation of bimodal value neurons in the macaque putamen, which converges value information from tactile and visual inputs, efficiently preserves both value and modality information through shared abstract representations. These population representations generalized across identical modalities and values, establishing and maintaining an efficient low-dimensional representation as the neural geometry dynamically shifted toward value-guided movement within a single trial. Interestingly, a faster transformation of this geometry into a shared-value representation in bimodal value neurons was associated with a cognitive state reflecting well-adapted and well-learned value-guided behavior. In contrast, this relationship was notably absent in unimodal value neurons. Our results indicate that bimodal value neurons in the putamen play a key role in balancing efficiency and information fidelity through shared neural representations, with their dynamic changes facilitating the cognitive states required for value-guided behavior.

Our brain processes numerous functions with a limited number of neurons, unlike contemporary artificial intelligence, which can expand its computing resources. This limitation is particularly prominent in cortico-basal ganglia circuits, where neuron numbers are significantly reduced, referred to as the anatomical funneling circuit¹⁻⁴. This anatomical arrangement suggests that striatal neurons might process multiple cortical inputs in a convergent manner¹⁻⁷. Interestingly, we have demonstrated this convergent processing, particularly when encoding reward value information across different modalities at the single-neuron level in the primate putamen⁸. Bimodal value neurons, which encode both tactile and visual value information, constituted

more than half of the value-coding neurons in the putamen, underscoring the striatum's ability to efficiently handle a variety of functions with fewer neurons. This indicates that the striatum employs an information processing strategy that is quantitatively efficient.

Pursuing quantitative efficiency alone does not guarantee the quality of the information; instead, it often compromises the quality. If bimodal value neurons encode both tactile and visual value information into a unified value representation without preserving their modality features, the result can be a decline in information quality⁸. This issue may be critical, particularly in conditions that require animals to rely on both modality and value information. Additionally,

¹School of Biological Sciences, College of Natural Sciences, Seoul National University (SNU), Seoul, Republic of Korea. ²Institute for Data Innovation in Science, Seoul National University (SNU), Seoul, Republic of Korea. ³Department of Biomedical Engineering, Ulsan National Institute of Science and Technology, Ulsan, Republic of Korea. ⁴These authors contributed equally: Seong-Hwan Hwang, Ji-Woo Lee. ✉ e-mail: hfkim@snu.ac.kr

such information may not be immediately necessary but could be useful in future learning and decision-making scenarios. Therefore, preserving the complete set of information could be beneficial for optimizing value-guided behavior in various environments. Based on this, we hypothesized that neurons in the putamen employ mechanisms to ensure both quantitative efficiency and the qualitative preservation of information.

Efficient information processing may involve generalizing multiple pieces of information based on shared features. Considering neuronal energy consumption, generating more neural patterns requires greater energy, as transitions between brain states involve synaptic changes, ion channel alterations, and structural modifications, all demanding an ATP supply⁹. Structured neural representations that leverage these shared features enable brain regions to process diverse information more concisely and efficiently within lower-dimensional neural representations^{10–13}. This abstract form of neural geometry has been observed in the prefrontal cortex and hippocampus, where it reflects the cognitive states of subjects^{11,14,15}. However, it remains unclear as to whether such abstract representations exist in the primate putamen within the basal ganglia system.

The putamen has traditionally been recognized for its role in motor control compared to other basal ganglia structures, primarily due to its anatomical inputs from the primary motor cortex (M1) and outputs to the globus pallidus internal segment, which in turn projects back to M1^{2,16–21}. However, putamen neurons also receive inputs from sensory regions, including the somatosensory cortex for tactile processing and the temporal cortex for visual processing, as well as dopaminergic input from the substantia nigra pars compacta^{22–24}. Reflecting these anatomical connections, studies have reported various roles of the putamen, including action value processing^{25,26}, object value processing^{27,28}, and learning^{29–31}. These findings suggest that the putamen plays a broader role beyond motor control, extending into cognitive processes such as value learning and behavioral adaptation potentially through sensory-to-value transformation.

Given its processing of motor, sensory, and value-related signals, fundamental questions remain: How does the putamen encode two different types of information, value and modality, at the population level? Does the putamen's population activity generate an efficient neural geometry through shared representations, and if so, how does this geometry dynamically transform across learning phases? Furthermore, which aspects of its neural representation most directly reflect and guide the cognitive states underlying adaptive value-guided movements?

In this study, we examined the neural geometry in the primate putamen, analyzing representations for each modality and value through cross-condition generalization performance (CCGP) outcomes using pseudo-populations¹⁰. Our findings revealed that bimodal value neurons efficiently encode both modality and value information with a low-dimensional representation, exhibiting dynamic changes in their geometric structures across task periods. We also conducted additional analyses to investigate whether these dynamic changes in neural geometry were correlated with cognitive states during the execution of value-guided behavior.

Results

Convergent processing of tactile and visual values in the primate putamen

To examine how the population of neurons in the primate putamen processes value information from tactile and visual inputs, we trained monkeys to perform both tactile and visual value reversal tasks, as previously described (Fig. 1A, B and Supplementary Fig. S1A)⁸. In the tactile and visual value reversal tasks (T-VRT and V-VRT), one braille pattern or fractal image was associated with a reward (good), and the other was not (bad). This stimulus-reward contingency was reversed after 40 trials, enabling the examination of

neural responses encoding the value while excluding neural responses to the stimuli (Fig. 1C).

In both tasks, the same tactile or visual stimulus was presented twice after the presentation of a square cue indicating finger insertion, enabling the monkeys to experience the stimulus during the first cue presentation (stimulus presentation period) and to predict the reward outcome during the blank delay period before the second cue presentation (Fig. 1B). Consequently, the monkeys inserted their fingers more rapidly into the hole after the second cue presentation when the previously experienced good stimulus was presented compared to the bad stimulus (Fig. 1D). Specifically, the monkeys inserted their fingers more slowly to bad stimuli in V-VRT than T-VRT, while they responded more quickly to good stimuli in T-VRT than V-VRT (Supplementary Fig. S1B). There were more give-up trials (i.e., trials in which the monkeys did not insert their fingers into the hole) when they encountered bad stimuli in V-VRT (Supplementary Fig. S1C). When assessing how quickly the monkeys adapted their behavior following a value reversal, their reaction times shifted rapidly within four trials for both good and bad stimuli in both tasks (Supplementary Fig. S1D, E). Overall, the difference in the reaction time indicates that the monkeys acquired and retained the values associated with the tactile and visual stimuli until the second cue presentation.

Three types of value-coding neurons were identified in the primate putamen through single-unit recording, as previously reported: tactile-selective value neurons, which respond specifically to tactile-related value information; visual-selective value neurons, which encode value information related to visual stimuli; and bimodal value neurons, which encode value information from both tactile and visual modalities (Fig. 1E)⁸. Bimodal value neurons comprise 43% of all task-related responsive neurons (129/299) and 52% of all value-coding neurons (129/247).

Notably, we observed that bimodal value neurons in the putamen showed value discrimination responses in both T-VRT and V-VRT, but these responses differed during the same periods and often occurred in entirely different periods (Fig. 1F, G and Supplementary Fig. S2A, B). Figure 1F shows an example neuron that exhibited stronger responses to good stimuli than to bad stimuli during the stimulus presentation period in both T-VRT and V-VRT, but its response patterns differed between the two tasks. Moreover, value encoding of the putamen neurons was often distributed across different task periods rather than confined to a single period (Supplementary Table S1). For instance, the neuron in Fig. 1G encoded both tactile and visual values, but it represented each value during different periods: the tactile value was encoded during the blank delay period while the visual value was encoded during the stimulus presentation period.

These bimodal value neurons recorded across all putamen areas exhibited heterogeneity during the processing of modality information: at the single-neuron level, 55% of bimodal value neurons encoded modality information, while 45% did not (Supplementary Fig. S2C). Bimodal value neurons did not show significant differences in the timing of value discrimination, but they exhibited a greater magnitude of value discrimination responses in V-VRT compared to T-VRT (Supplementary Fig. S2D, E).

For a more thorough exploration of how bimodal value neurons encode modality and value, we calculated the pairwise correlation of regression coefficients for each unit (Fig. 1H). These results showed no statistically significant correlation between modality and value responses ($p = 0.15$, Pearson's correlation), indicating that these representations are highly separable.

Given that the putamen is known to play a role in motor movements^{25,32,33}, we further examined whether eye, finger, and arm movements could be classified based on the reward value during T-VRT and V-VRT. However, our analysis revealed that the monkeys did not adjust their eye, finger, or arm movements according to either reward value or modality, indicating that bimodal value neurons

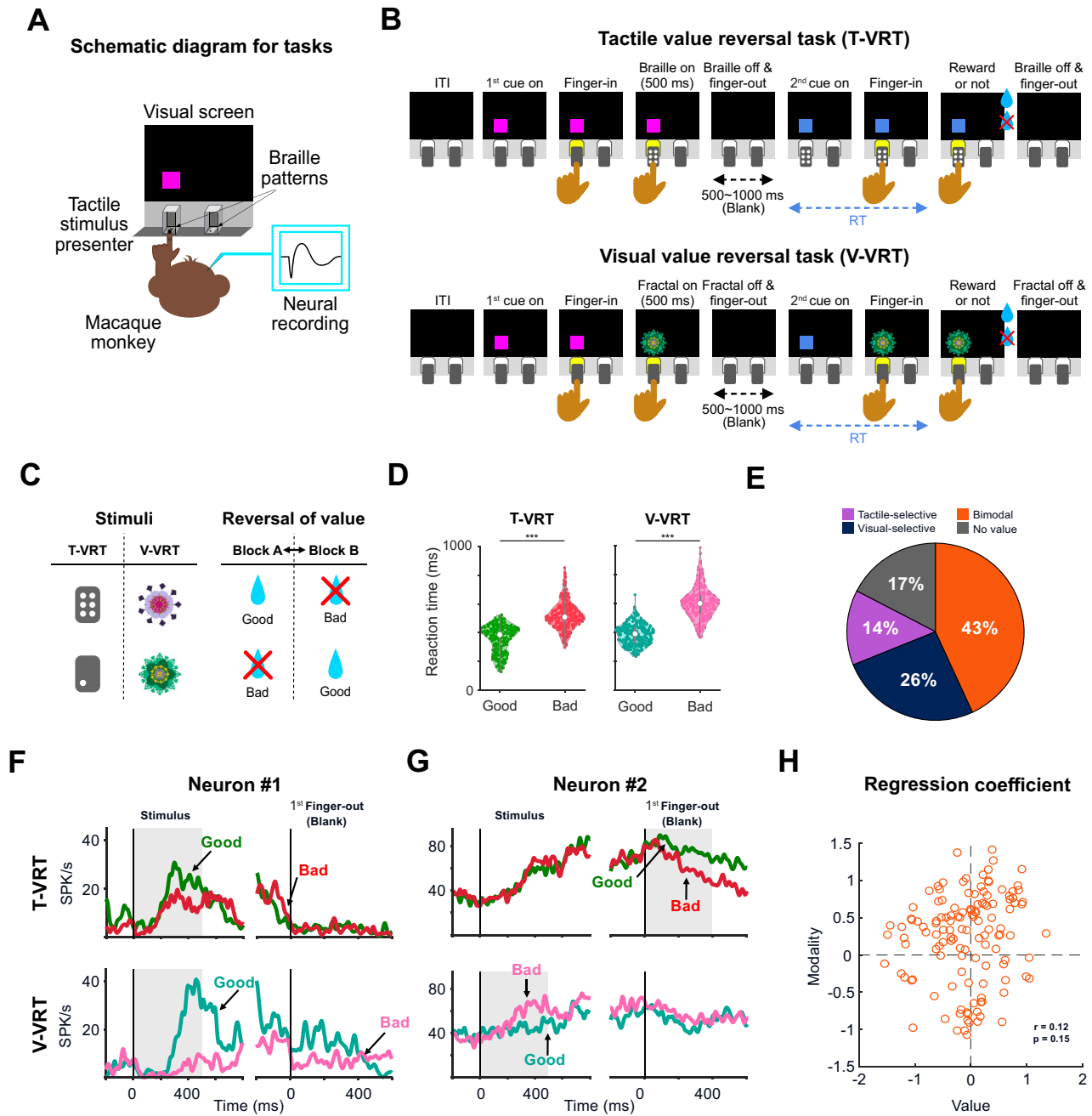


Fig. 1 | Tactile and visual value-guided finger-insertion behavior and heterogeneous responses of bimodal value neurons in the primate putamen. **A** A diagram illustrating the experimental setup for macaque monkeys. Tactile stimuli were delivered via a tactile presenter, and visual stimuli were presented on a monitor screen when the monkey inserted its finger into the tactile stimulus presentation box. Neural activities in the putamen were recorded as the monkey performed the tasks. **B** Procedures of two different modality value reversal tasks: referred to here as the Tactile Value Reversal Task (T-VRT) and the Visual Value Reversal Task (V-VRT). The two tasks are identical in terms of the procedure, with the only difference being the type of stimuli presented. **C** In T-VRT, braille patterns were used as tactile stimuli. In V-VRT, fractal images were used as visual stimuli. To avoid confusion in neural responses to the stimulus and value, reversal of the value was applied. **D** Differences in reaction times for finger insertion after the onset of the second cue based on stimulus-associated value ($n = 299$ sessions for both T-VRT and V-VRT, collected from two monkeys). Two-sided Wilcoxon signed-rank test was

used for T-VRT ($p = 8.866 \times 10^{-51}$) and two-sided paired t-test for V-VRT ($p = 1.393 \times 10^{-114}$) ($***p < 0.0005$). The solid thick gray bar in the center of each violin plot represents the interquartile range (from the 1st to the 3rd quartile), and the thin line shows the data range excluding outliers. The white circle within each plot indicates the median value. **E** Pie chart of recorded neurons in the putamen ($n = 299$). **F** Responses of an example bimodal value neuron in the putamen in T-VRT and V-VRT. SPK/s: spikes per second. **G** Responses of another bimodal value neuron as an example. SPK/s: spikes per second. **H** The pairwise relationship between regression coefficients for modality and value in bimodal value neurons ($n = 129$). A two-sided Pearson's correlation test was used to assess statistical significance. Figure 1B, C adapted from Hwang, SH., Park, D., Lee, JW. et al. Convergent representation of values from tactile and visual inputs for efficient goal-directed behavior in the primate putamen. Nat. Commun. 15, 8954 (2024). <https://doi.org/10.1038/s41467-024-53342-x>.

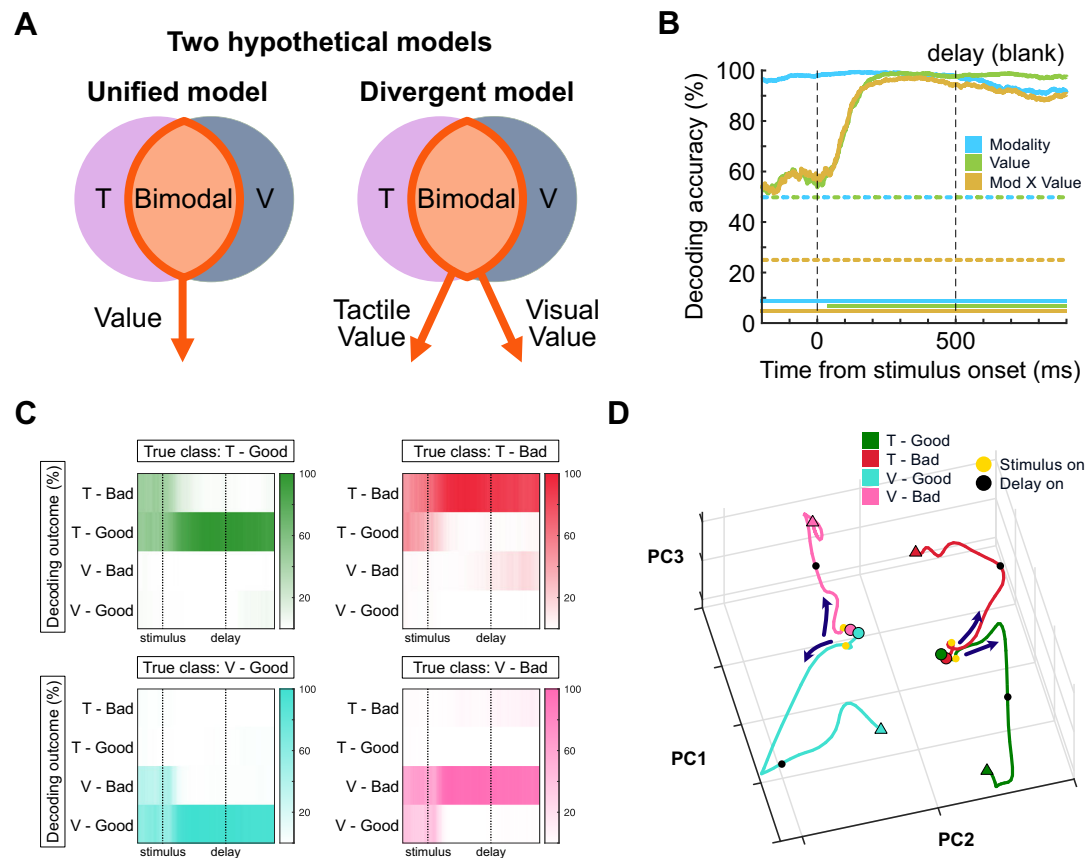


Fig. 2 | The neural ensemble of bimodal value neurons in the putamen represents both modality and value information. **A** Illustration of two hypotheses of the way bimodal value neurons process both modality and value information. **B** Decoding performance plotted as a function of time for each variable in bimodal value neurons: modality, value, and the interaction between modality and value. Horizontal bars represent periods of decoding accuracy above the permutation results (right-tailed z-test, $p < 0.05$). **C** Confusion matrix for four different

conditions. Each graph has a different class variable and shows the responses of the decoder. T tactile, V Visual. **D** An example of neural trajectories of bimodal value neurons (Monkey EV) in the subspace projected to the first three principal components (PCs). The circle and triangle denote the start (-200 ms from the stimulus onset) and end points (1000 ms from the stimulus onset), respectively. Yellow and dark circles indicate the stimulus-on and delay-on points, respectively.

encode value and modality independently of these motor-related factors (Supplementary Fig. S3). Taken together, although nearly half of value-coding neurons encode both tactile and visual value information, the manner in which that information is encoded has heterogeneous response profiles across different task periods.

The population patterns of bimodal value neurons represent tactile and visual values

Previous studies have suggested that complex neural activities may serve latent functions related to the processing of various types of information, which can be elucidated through population-level analyses^{34–37}. The diversity in value encoding at the single-neuron level raises a question about the corresponding population-level responses (Fig. 2A): Do the population patterns of these neurons encode value information from tactile and visual inputs into a unified value, or do they separately represent the tactile and visual values? To determine whether bimodal value neurons process each value separately or in a unified manner, we conducted population decoding analyses of bimodal value neurons using three variables: modality, value, and their interaction (Fig. 2B and Supplementary Fig. S4A).

The decoding accuracy for value was at the chance level (50%) before the onset of the stimulus, but it quickly started to increase as the stimulus was presented. In contrast, modality was decoded with nearly 100% accuracy prior to stimulus onset, suggesting that bimodal

value neurons process modality information similarly to how contextual information is processed in each task. The decoding accuracy for the interaction between value and modality (Tactile-good value/Tactile-bad value/Visual-good value/Visual-bad value) also increased and reached nearly 100% after stimulus presentation, but the accuracy was already around 50% even before the stimulus was presented (chance level = 25%). Considering that the bimodal value neurons represented the modality from the beginning of the trials, this statistically significant decoding for interaction prior to stimulus onset may be due to the use of modality information. To test this possibility, we constructed a confusion matrix of the decoder testing interaction between value and modality. These results indicate that the decoder differentiated between tactile and visual modalities prior to stimulus onset, and began discriminating values specific to each modality condition after stimulus presentation (Fig. 2C). This suggests that bimodal value neurons process modality as contextual information and selectively discriminate values within each modality condition.

These neural representations of modality and value dynamically changed over time (Fig. 2D). We compared the dynamics of the population activity among four conditions representing the combinations of modality and value in the subspace projected to the first three principal components (PCs) (Fig. 2D and Supplementary Fig. S4B, C). Consistent with the decoding results, the trajectories revealed

that the patterns of dynamics in the latent space initially clustered by modality and then diverged according to their value and modality after stimulus presentation. Notably, the trajectories for good values moved nearly in parallel along the same direction, while those for bad values moved in parallel but in the opposite direction, suggesting an abstract representation of value (Fig. 2D). Overall, our data indicate that bimodal value neurons represented value differently depending on its modality, suggesting that the neural population in the putamen maintained the unique feature of modality when processing value components, supporting the divergent model in Fig. 2A.

Dynamic changes of the neural geometry during the processing of value and modality

This distinct process of tactile and visual values at the population level of bimodal value neurons raises a question: Do bimodal value neurons encode value and modality in a structured representation, and can it be generalized through shared features? If multiple variables can be generalized with a shared feature, the corresponding neural geometry forms an ‘abstract representation’, allowing for a reduction of the neural dimensions when processing multiple inputs^{10,11,38,39}.

To investigate this, we measured how well each variable is generalized using the cross-condition generalization performance (CCGP), following previously established methods¹⁰. In the CCGP analysis, we determined whether a decoder, trained to identify the value (or modality) in one of two conditions (e.g., the good or bad in tactile condition), could decode the same value (or modality) in a condition not used for the training of the decoder (e.g., good or bad in the visual condition) (Fig. 3A).

Figure 3B illustrates the dynamic change of the CCGPs for value and modality as the trial progresses, aligned with the stimulus presentation (see also Supplementary Fig. S5A, B). The CCGP for modality was initially above the chance level and sustained this level until -150 ms after stimulus presentation. In contrast, the CCGP for value increased after stimulus onset, surpassing the chance level 230 ms after the stimulus appeared. The CCGP for value continued to rise after stimulus onset and during the delay period, while the CCGP for modality continued to decline during stimulus onset and at the beginning of the delay period.

Overall, the CCGPs for value and modality were initially distinct and then became similar, eventually reversing as the trial progressed. To provide clear verification and visualization of this observation, we divided the time window of the trial into three distinct phases: Phase 1, which encompasses the prestimulus-early stimulus periods, from -200 to 150 ms aligned with the stimulus onset; Phase 2, focusing on stimulus presentation, from 150 to 500 ms; and Phase 3, covering the blank delay period, from 500 to 1000 ms (For further details and the rationale behind this segmentation, refer to the methods section). We also analyzed these three phases by determining which variables (value and modality) were generalized across shared features in each phase (Fig. 3C and Supplementary Fig. S5C). In phase 1, the CCGP for modality was above the chance level, whereas for value it was not (Fig. 3C, left panel). In both phases 2 and 3, the decoding accuracy for the interaction between value and modality exceeded 98%, as analyzed by a traditional linear decoder (Fig. 3C, middle and right panels). However, the extent of the generalized representation dynamically changed as the phase progressed. In phase 2, the CCGPs for both value and modality were above the chance level (Fig. 3C, middle panel). However, in phase 3, the extent of the generalized representation for value increased further, but the extent of the generalized representation for modality decreased to the chance level, as analyzed according to the CCGP (Fig. 3C, right panel).

For more clarification of the representational geometry of bimodal value neurons, we also computed the parallelism score (PS) in each phase, as previously reported, to quantify the degree to which the coding directions are parallel¹⁰. If the coding vectors for each variable

are nearly parallel, the PS will deviate significantly from 0. Conversely, if the neural representations of each variable are similar to random representations, the PS will be approximately 0, indicating orthogonality between the coding vectors. In this study, we can obtain coding vectors for classifiers trained to classify values as tactile-good and tactile-bad, as well as classifiers trained to classify values as visual-good and visual-bad. We can then calculate the cosine angle between these two coding vectors and define it as the PS for ‘value’. A cosine angle between these two coding vectors close to 1 indicates that the two vectors are parallel.

As shown in the results depicted in Fig. 3C, the PSs for value and modality in all phases were above the chance level, except for the PS for value in phase 1. This suggests that the coding directions for both modality and value are almost parallel to the coding direction for that same variable across conditions after stimulus onset, potentially leading to high decoding accuracy rates and CCGPs in phases 2 and 3. Taken together, our quantification analyses using the CCGP revealed that as the trial progressed toward value-guided movements, the generalized representation for modality decreased, whereas the generalized representation for value increased.

To visualize the geometric architecture of these neural representations, the average population activities for all four possible pairings of value and modality in each phase were projected into a three-dimensional principal component (PC) space (Fig. 3D and Supplementary Movie 1). In phase 1, the population activities clustered according to the modality, showing similar representation outcomes across the same modality. Interestingly, as they progressed to phase 2, each variable diverged, forming a square-shaped geometry that captures low-dimensional representations for both value and modality. Subsequently, this geometric arrangement stretched along the value axis during the delay period of phase 3, resulting in a rectangular-shaped geometry that reflects stronger similarity in representations for the same values compared to the same modalities (Supplementary Fig. S5D). Our comprehensive analytical approaches, including CCGP and population responses in latent dimensions, successfully demonstrated that bimodal value neurons form low-dimensional representations. Furthermore, this neural geometry exhibited dynamic changes as the trial progressed, primarily stretching out along the value axis (Fig. 3D and Supplementary Fig. S5D).

The representational geometry for value and modality is correlated with the performance of value-guided behavior

The ensemble of bimodal value neurons in the putamen dynamically shifted towards enhancing the generalized representation of value when value-guided behavior is imminent. Accordingly, we investigated whether this dynamic shift was correlated with the performance of the value-guided behavior.

To assess this, we categorized trials based on reaction times during finger insertion, dividing them into adapted and unadapted behavior trials (Fig. 4A). Because the values of tactile and visual stimuli were reversed in each block, the monkeys had to learn and adjust their finger-insertion movements accordingly. Indeed, the monkeys exhibited adaptive behavior: their finger movements became faster for good stimuli and slower for bad stimuli (Supplementary Fig. S1D, E). Therefore, we defined adapted behavior trials as those in which the reaction times clearly differentiated between values—faster for good stimuli and slower for bad stimuli—falling above or below the 50th percentile, respectively. In contrast, unadapted behavior trials included those in which the reaction times did not clearly differentiate between values—slower for good stimuli and faster for bad stimuli—falling in the lower and upper portions of the 50th percentile, respectively. This classification allowed us to examine how population-level neural representations differed when monkeys adapted to value changes and exhibited clear value-based behaviors versus when their behavior remained ambiguous.

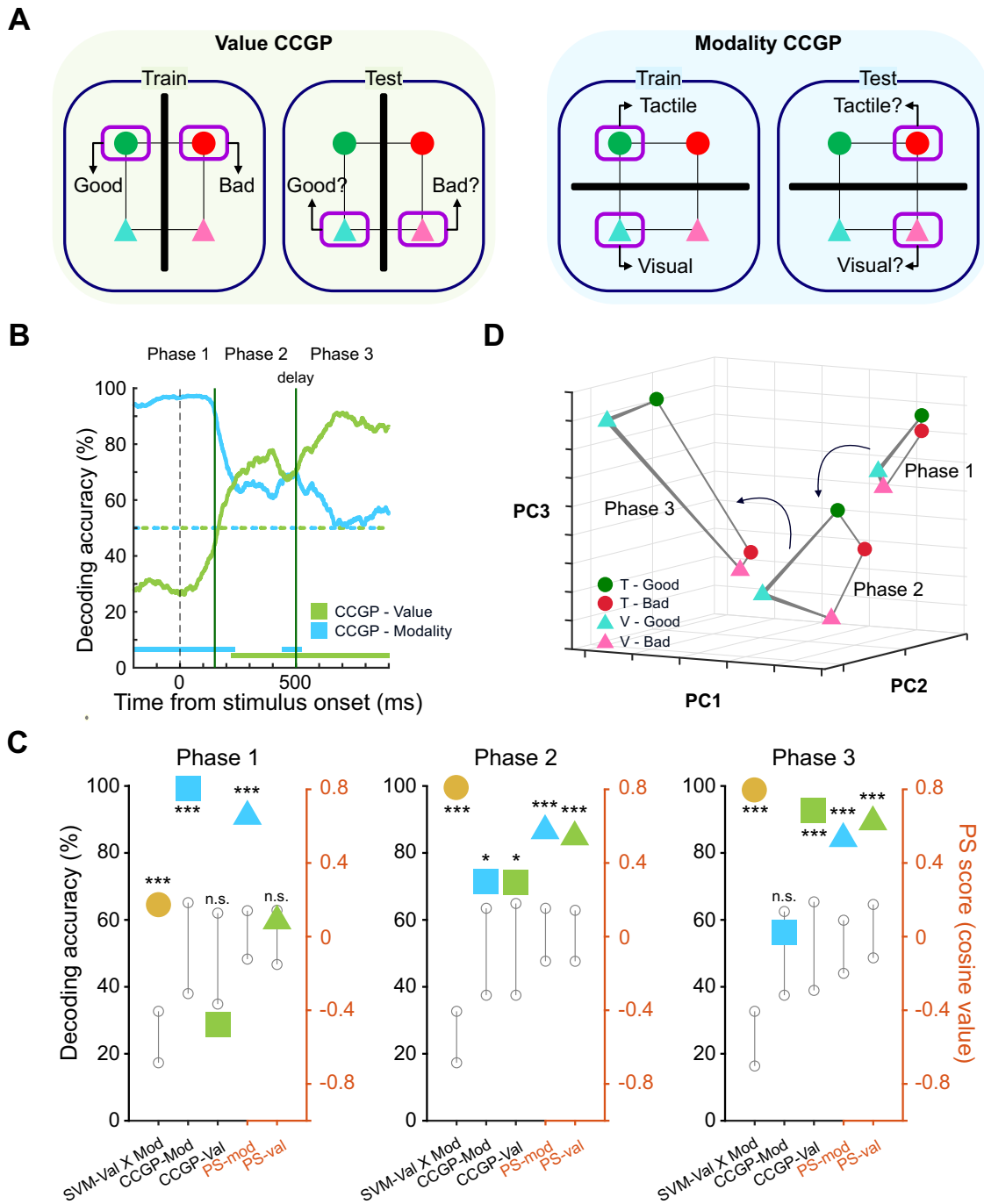
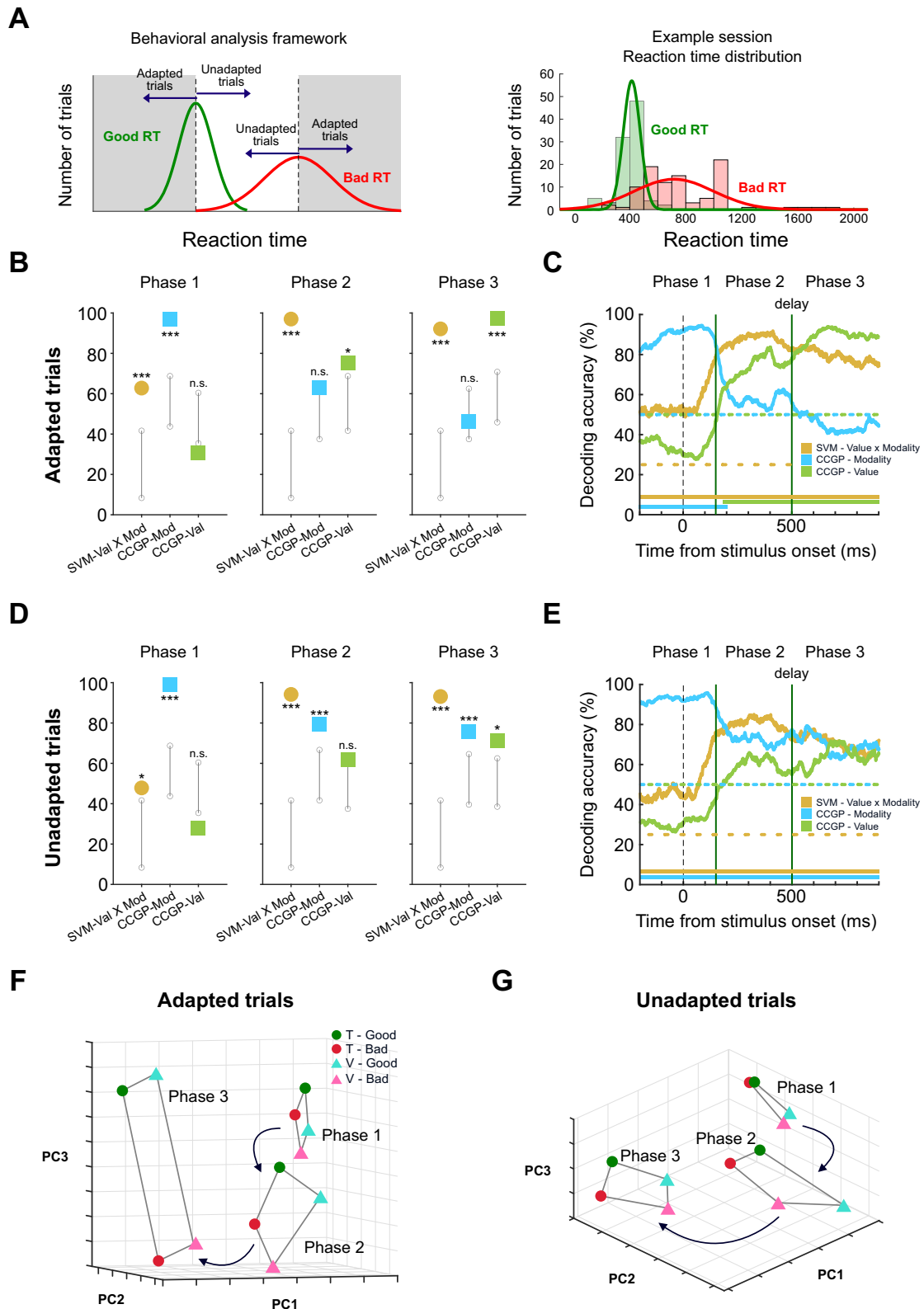


Fig. 3 | Dynamic changes in the generalized representation of bimodal value neurons in the putamen over time. **A** CCGP scheme for modality and value. Green and red circles indicate tactile-good and tactile-bad conditions, respectively. Cyan and pink triangles indicate visual-good and visual-bad conditions, respectively. Different conditions were trained and tested to measure the extent of the generalization of each variable. **B** CCGP plotted as a function of time for value and modality information in bimodal value neurons. Horizontal bars represent periods of decoding performance above the results of the null model (right-tailed z-test,

$p < 0.05$). **C** Comprehensive results of three analytic approaches (traditional decoding using SVM, CCGP, and PS) in three different time phases. The colored indicators represent the mean of each result, while the grayscale vertical bars with open circles indicate the 95% confidence interval of the null model. P values derived from the Z score of data compared to the null model are also shown (right-tailed for SVM and CCGP, two-tailed for PS). **D** Principal component analysis (PCA) plot depicting the representational geometry of bimodal value neurons over time with respect to value and modality. * $p < 0.05$, *** $p < 0.0005$, n.s. not significant.

A traditional population decoding analysis for the interaction between modality and value showed no clear difference between the two groups across all phases. Particularly in phase 2 and phase 3, after the monkeys experienced the value-associated stimulus, the decoding accuracy approached 100% in both groups (Fig. 4B, D, Supplementary Fig. S6A, C). However, these two groups showed clear differences in

the generalized representations of value and modality as the finger-insertion progressed. The CCGPs for modality were statistically significant in both groups during phase 1. However, distinct changes emerged between the groups in phases 2 and 3. In the adapted behavior trials, the CCGP for modality dropped to the chance level in phase 2, while the CCGP for value increased above chance in phase 2,



reaching nearly 100% accuracy in phase 3 (Fig. 4B). Conversely, for the unadapted behavior trials, the CCGP for modality remained above the chance level across all phases. Meanwhile, the CCGP for value remained at the chance level through phase 2 and only slightly exceeded the chance level in phase 3 (Fig. 4D). Additional statistical analyses showed modality CCGP for unadapted trials was higher than

those for adapted trials, whereas value CCGP for adapted trials was higher than that for unadapted trials during phases 2 and 3 (Supplementary Fig. S6E). Time-resolved decoding analyses confirmed that the differences between the two groups were driven by the extent of the generalization of modality and value, as opposed to traditional decoding performance (Fig. 4C, E). The different neural representation

Fig. 4 | Relationship between adaptive behavior performance and the geometry of neural representation. **A** Analytic scheme for dividing trials into the adapted and unadapted finger-in reaction time. A histogram of reaction times in the actual example session is shown in the panel on the right. **B** Comprehensive results of traditional decoding (SVM) and CCGP in three different time phases with adapted behavior trials. The colored indicators represent the mean of each result, while the grayscale vertical bars with open circles indicate the 95% confidence interval of the null model (right-tailed z-test). **C** Traditional decoding (SVM) and

CCGP with adapted behavior trials plotted as a function of time. Horizontal bars represent periods of decoding performance above the results of the null model (right-tailed z-test, $p < 0.05$). **D** Identical to **(B)** but for unadapted behavior trials (right-tailed z-test). **E** Identical to **(C)** but for unadapted behavior trials (right-tailed z-test, $p < 0.05$). **F** Principal component analysis (PCA) plot illustrating the geometry of bimodal value neurons over time with adapted behavior trials. **G** The same format is used for **(F)** but with unadapted behavior trials. * $p < 0.05$, *** $p < 0.0005$, n.s. not significant.

outcomes between the adapted and unadapted behavior trials persisted even after the delay period (Supplementary Fig. S6B, D).

This difference between the groups is visualized by projecting the average population activity for all possible pairings of value and modality into a three-dimensional latent space (Fig. 4F, G and Supplementary Fig. S6F). The neural geometries of adapted and unadapted behavior trials, which were initially more clustered together in phase 1, gradually diverged between the trial groups as the trial progressed (Supplementary Fig. S6G). The neural geometry of adapted behavior trials stretched out more extremely along the value axis as the phases progressed compared to the unadapted behavior trials (Fig. 4F, G and Supplementary Fig. S6H). Together, these results suggest that value-guided adaptive behavior is more strongly linked to the extent of neural pattern generalization within the same value category than to the distinct encoding of modality and value information.

Neural geometry dynamics reflect cognitive states associated with different learning stages

Recent studies have shown that changes in the neural geometry may be linked to shifts in cognitive states related to learning and memory^{11,14}. Given prior findings that the putamen plays a role in object-value associative learning^{27,29,40}, we examined whether the transformation of the neural geometry in the putamen differs across learning stages in the T-VRT and V-VRT.

As object-value associative learning progressed, the monkeys' reaction times changed across the learning stages (Fig. 5A). During the early learning stage, defined as the first half of the trials in each block, the difference in the finger-insertion reaction times between good and bad stimuli was smaller compared to that in the late learning stage, which consisted of the last half of the trials in each block (Fig. 5B).

To investigate how the neural geometry in the putamen evolves differently across learning stages, we conducted the same analysis used in Fig. 4. First, we analyzed the traditional decoding accuracy for value and modality, finding that it remained high during phases 2 and 3 in both the early and late learning stages (Fig. 5C–F). Interestingly, a key difference between the two learning stages emerged in the CCGP analysis. In the early learning stage, the CCGP for value remained at the chance level throughout all phases (Fig. 5C, D); however, in the late learning stage, it exceeded the chance level from phase 2 onward (Fig. 5E, F). Further statistical analyses confirmed that modality CCGP was higher in the early stage than in the late stage, whereas value CCGP was higher in the late stage compared to the early stage during phases 2 and 3 (Supplementary Fig. S7A). This finding demonstrates that as value learning progresses, the neural population shifts toward a more abstract value representation.

This conclusion was further supported by latent space projections of population activity (Fig. 5G, H and Supplementary Fig. S7B–D). The neural geometries of early and late learning stages, which were more clustered together in phase 1, gradually diverged between the two learning stages as the trial progressed (Supplementary Fig. S7C). In the early learning stage, the neural representations of the same modalities became more closely clustered than the same values, whereas in the late learning stage, the neural representations of the same values became more closely clustered than the same modalities (Supplementary Fig. S7D). Taken together with the previous analyses of the adapted and unadapted behavior trials, the transformation of the

neural geometry in the putamen reflects cognitive states related to how well the monkeys recognize and utilize learned values to guide value-driven behavior.

Distinct contribution of two types of bimodal value neurons to the generalized representation of value and modality

In our previous study, we identified two types of bimodal value neurons in the putamen, classified based on the periods of their strongest value responses: stimulus value neurons, which displayed the highest value discrimination responses during the stimulus presentation period, and delay value neurons, which exhibited the strongest value discrimination responses during the delay period⁸. To investigate the distinct roles of these two types of bimodal value neurons in processing value and modality at the population level, decoding analyses were conducted exclusively on neurons from each group (Fig. 6A, B and Supplementary Fig. S8A–C).

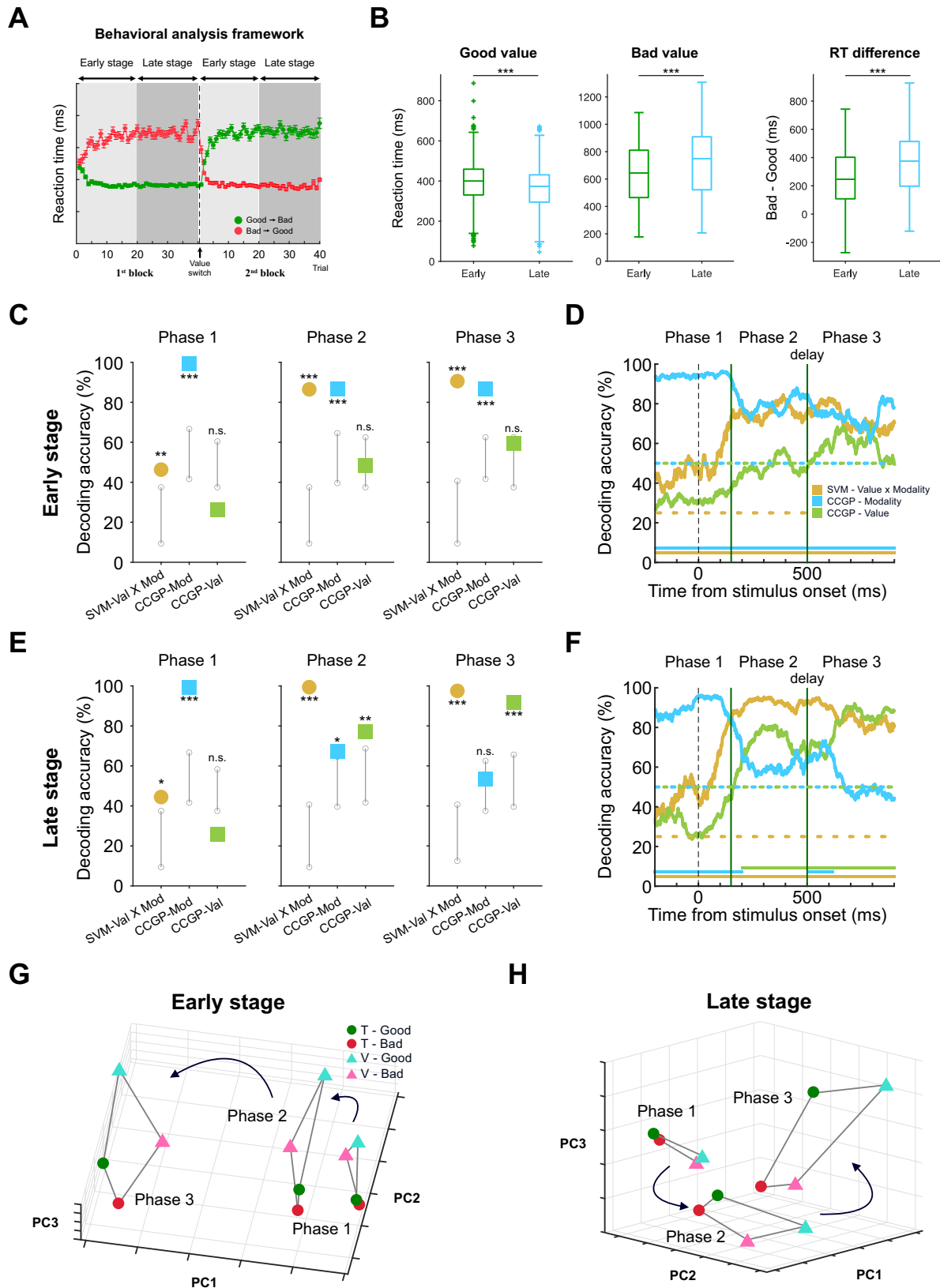
In traditional neural decoding, the decoding accuracy for the interaction between value and modality was robustly similar across any of the phases (Fig. 6A, B), suggesting that both subpopulations contributed similarly to processing value and modality information. However, the CCGP analysis revealed differences in the dynamic changes of the generalized representation for value and modality between these two types of bimodal value neurons.

In phase 1, both types of value-coding neurons exhibited high CCGPs for modality above the chance level, while the CCGPs for value were not statistically significant (Fig. 6A, B, left panels). In phase 2, the CCGP for value in stimulus value neurons rose above the chance level, while the CCGP for modality dropped to the chance level (Fig. 6A, middle panel). By phase 3, their CCGPs for both value and modality were no longer statistically significant (Fig. 6A, right panel). Conversely, in the delay value neurons, the CCGP for modality remained statistically significant in phase 2, while the CCGP for value did not (Fig. 6B, middle panel). In phase 3, this trend was reversed, with the CCGPs for value becoming significant and the CCGP for modality no longer being statistically significant (Fig. 6B, right panel).

We also observed distinct changes in the geometries of each neural type when projected into a three-dimensional latent space (Fig. 6C, D and Supplementary Fig. S8D). In phase 1, the population responses of stimulus value neurons clustered according to the contextual modality, reflecting a generalized representation of modality (Fig. 6C). In phase 2, their population responses stretched along the value axis, forming a rectangular-shaped geometry that captured the generalized representation of value. By phase 3, this geometry collapsed, resembling a random representation.

In contrast, the population responses of delay value neurons maintained their clustering according to the contextual modality until phase 2 (Fig. 6D and Supplementary Fig. S8D). However, in phase 3, these responses diverged along the value axis, forming a rectangular-shaped geometry.

Overall, both types of value neurons demonstrated similar capacities for conveying value and modality information but exhibited distinct dynamic changes in their neural representations of modality and value. This ablation study, which excluded one neural type at a time, revealed that both types of neurons in the putamen were essential for generating the factorized representation observed in phase 2, as shown in Fig. 3C.



Selective generalized representation for modality but not value by modality-selective value neurons

Modality-selective value neurons, which selectively encode either tactile or visual value, constitute the remaining half of the value-coding neurons identified in the putamen. We investigated their contributions to the generalized representation of value and modality as well as their

correlation with value-guided behavior at the population level (Fig. 7A).

Our findings revealed that the population activity of modality-selective value neurons selectively represented the generalized form of modality but not the value across all phases (Fig. 7B). In the traditional neural decoding analysis, these neurons successfully

Fig. 5 | Relationship between learning stage and the geometry of neural representation. **A** Behavioral analysis scheme for categorizing trials into early and late learning stages within each block. Reaction times (RT) for good (green) and bad (red) values are plotted across the trials. Shaded areas indicate early (light gray) and late (dark gray) learning stages. Each data point is based on a sample size ranging from 86 to 271 for the ‘Good → Bad’ condition, and from 73 to 271 for the ‘Bad → Good’ condition. The solid circles represent the mean reaction time across trials, and the error bars indicate the standard error of the mean (SEM) at each trial. **B** Box plots comparing the reaction times (RT) for good and bad values, as well as the RT difference (bad - good), between the early and late learning stages. A right-tailed Wilcoxon signed-rank test was conducted for the good value ($p = 6.497 \times 10^{-25}$), a left-tailed Wilcoxon signed-rank test for the bad value ($p = 1.94 \times 10^{-31}$), and a two-tailed Wilcoxon signed-rank test for the RT difference ($p = 3.709 \times 10^{-44}$) ($n = 997$ trials for both early and late). In box plots, the center line indicates the median, box

edges show the 25th and 75th percentiles, and whiskers extend to values within 1.5 times the interquartile range (IQR). Outliers beyond this range are shown as individual points. **C** Decoding results (SVM and CCGP) for modality and value in the early learning stage across three phases (right-tailed z-test). **D** Traditional decoding (SVM) and CCGP in the early learning stage are plotted as a function of time. Horizontal bars represent periods of decoding performance above the results of the null model (right-tailed z-test, $p < 0.05$). **E** Decoding results (SVM and CCGP) for modality and value in the late learning stage across three phases (right-tailed z-test). **F** Identical to (**D**) but for the late learning stage (right-tailed z-test, $p < 0.05$). **G** Principal component analysis (PCA) plot illustrating the geometry of bimodal value neurons over time in the early learning stage. **H** The same format is used in (**G**), but for the late learning stage. * $p < 0.05$, ** $p < 0.005$, *** $p < 0.0005$, n.s. not significant.

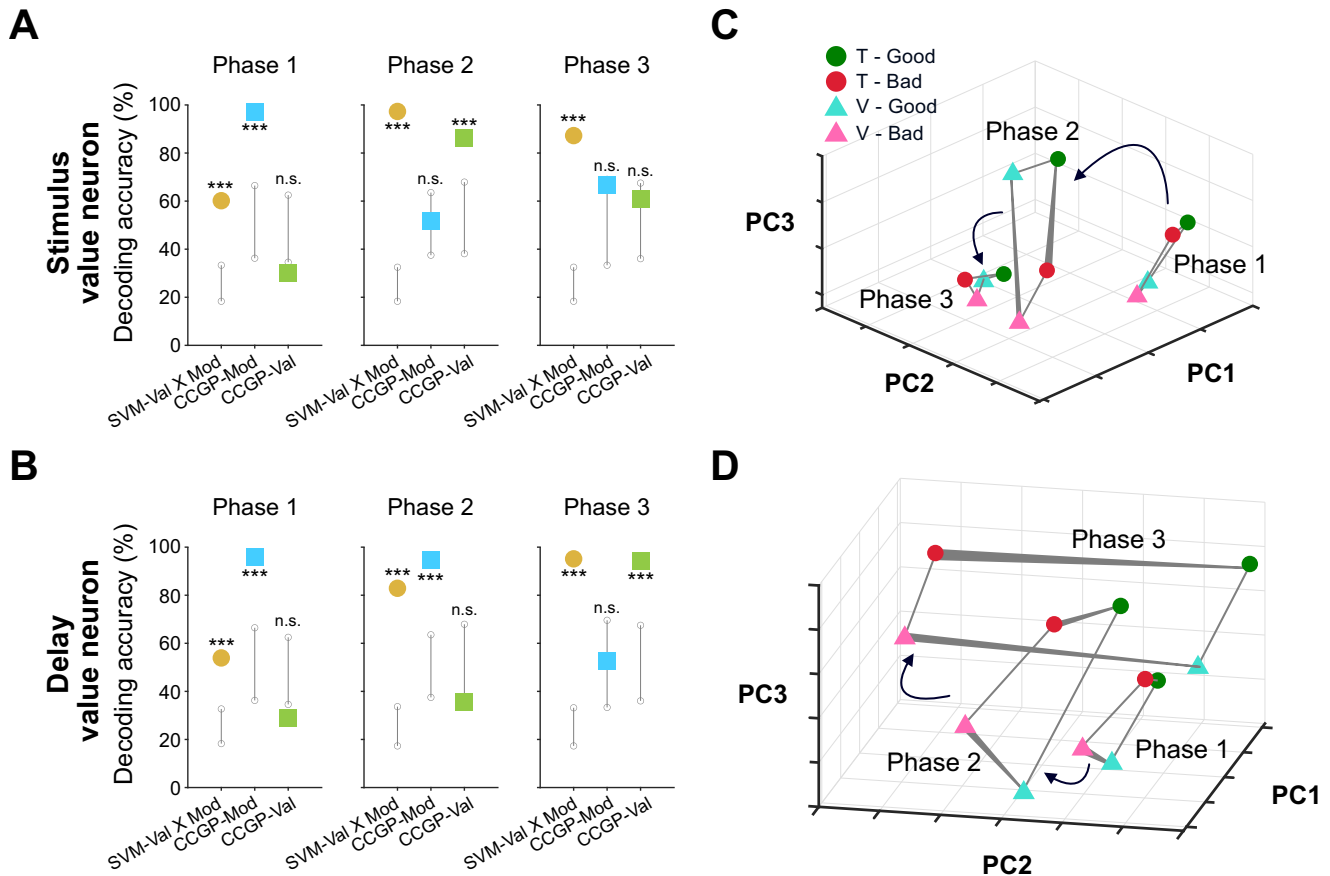


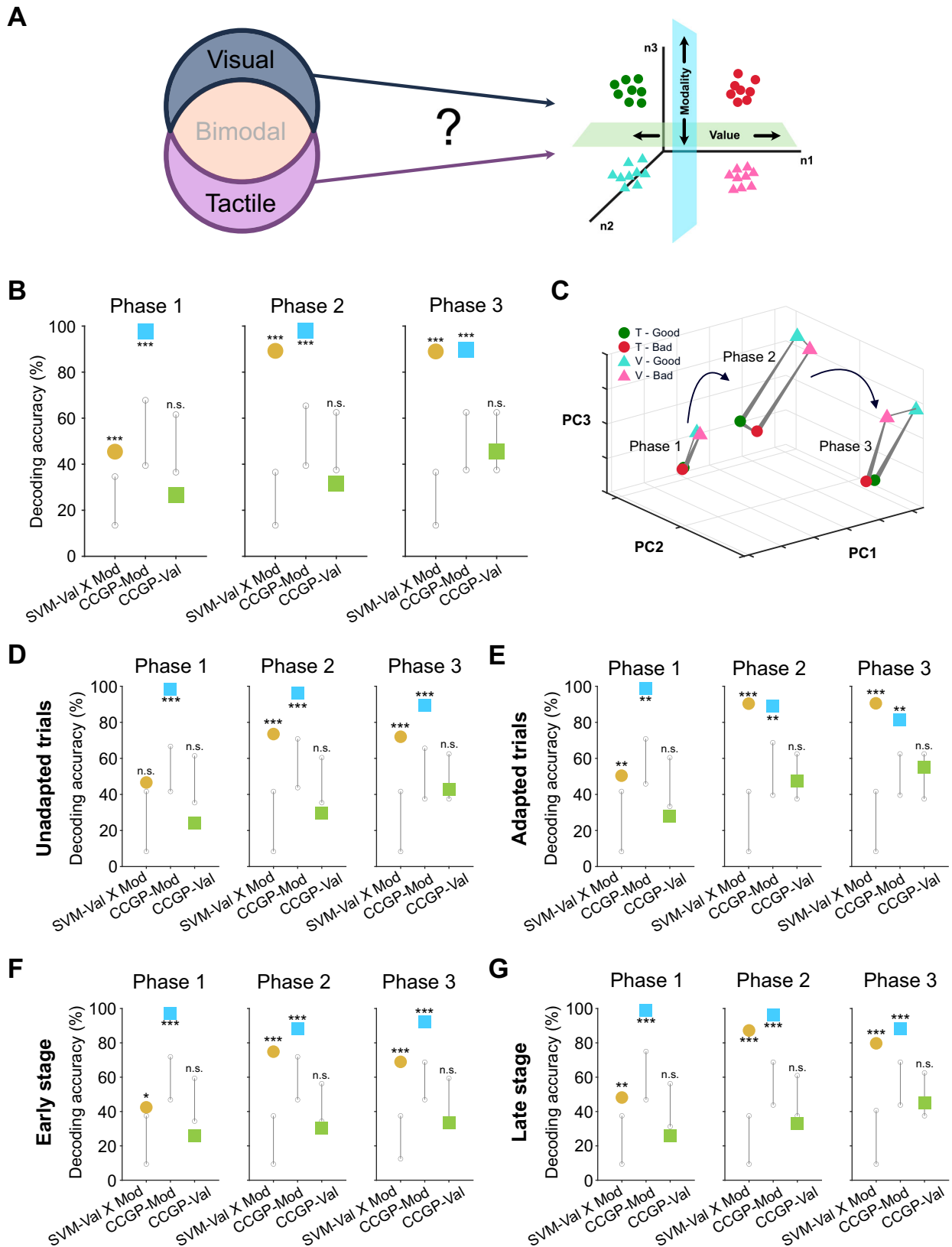
Fig. 6 | Subpopulations of bimodal value neurons contribute to different aspects of the neural geometry. **A** Traditional decoding performance (SVM) and CCGP for stimulus value neurons ($n = 55$) (right-tailed z-test). **B** The same format used in (**A**) but with delay value neurons ($n = 74$) (right-tailed z-test). **C** PCA plot

depicting the representational geometry of stimulus value neurons with respect to value and modality. **D** The same format is used in (**C**) but with delay value neurons. *** $p < 0.0005$, n.s. not significant.

discriminated value, modality, and their interaction during phases 2 and 3 (Fig. 7B and Supplementary Fig. S9A). However, their CCGPs for modality were consistently above the chance level, whereas those for value were not significant across all phases. In the visualization of neural representation changes projected into a three-dimensional latent space, the clustering according to modality was preserved across all phases (Fig. 7C).

To examine whether these dynamics of modality-selective value neurons were associated with behavioral performance, we analyzed the relationship between value-guided behaviors and changes in shared representation. In traditional neural decoding, the

performance accuracy rates in both phases 2 and 3 for both adapted and unadapted behavior trials were above the chance level (Fig. 7D, E). Furthermore, the dynamic changes of generalized representation were similar between the adapted and unadapted behavior trials: the CCGPs for modality were maintained across all three phases, while the CCGPs for value were not in both groups (Fig. 7D, E and Supplementary Fig. S9B–E). Likewise, a similar decoding pattern was observed across different learning stages (Fig. 7F, G and Supplementary Fig. S10). These findings suggest that modality-selective value neurons play a specialized role in generalizing modality information rather than value.



Discussion

Our population analyses demonstrated that bimodal value neurons in the putamen, which converge value information regardless of modality inputs at the single-neuron level, maintain distinct population representation for both modality and value information. These neurons exhibited a well-organized geometric structure, with shared

representations for identical modalities and values. Our findings suggest that neurons in the putamen form a low-dimensional population representation that efficiently preserves both value and modality information. Moreover, as the trials progressed, the neural geometry was dynamically transformed. Notably, a more rapid shift toward a shared-value representation in bimodal value neurons was associated

Fig. 7 | The selective role of modality-selective value neurons appears in the generalization of modality information, but not in the generalization of value. **A** Illustration of modality-selective value neurons when processing two different types of value information. We conducted the same analyses previously performed for bimodal value neurons using modality-selective value neurons. **B** Traditional decoding performance outcomes (SVM) and CCGP for modality-selective value neurons (right-tailed z-test). **C** PCA plot depicting the geometric structure of modality-selective value neurons with respect to value and modality. **D** Comprehensive results of traditional decoding and CCGP in three different time

phases with unadapted trials of modality-selective value neurons. The colored indicators represent the mean of each result, while the grayscale vertical bars with open circles indicate the 95% confidence interval of the null model (right-tailed z-test). **E** The same format used in (D) but with adapted trials (right-tailed z-test). **F** Decoding results (SVM and CCGP) for modality and value in the early learning stage across three phases (right-tailed z-test). **G** The same format used in (F) but in the late learning stages (right-tailed z-test). * $p < 0.05$, ** $p < 0.005$, *** $p < 0.0005$, n.s. not significant.

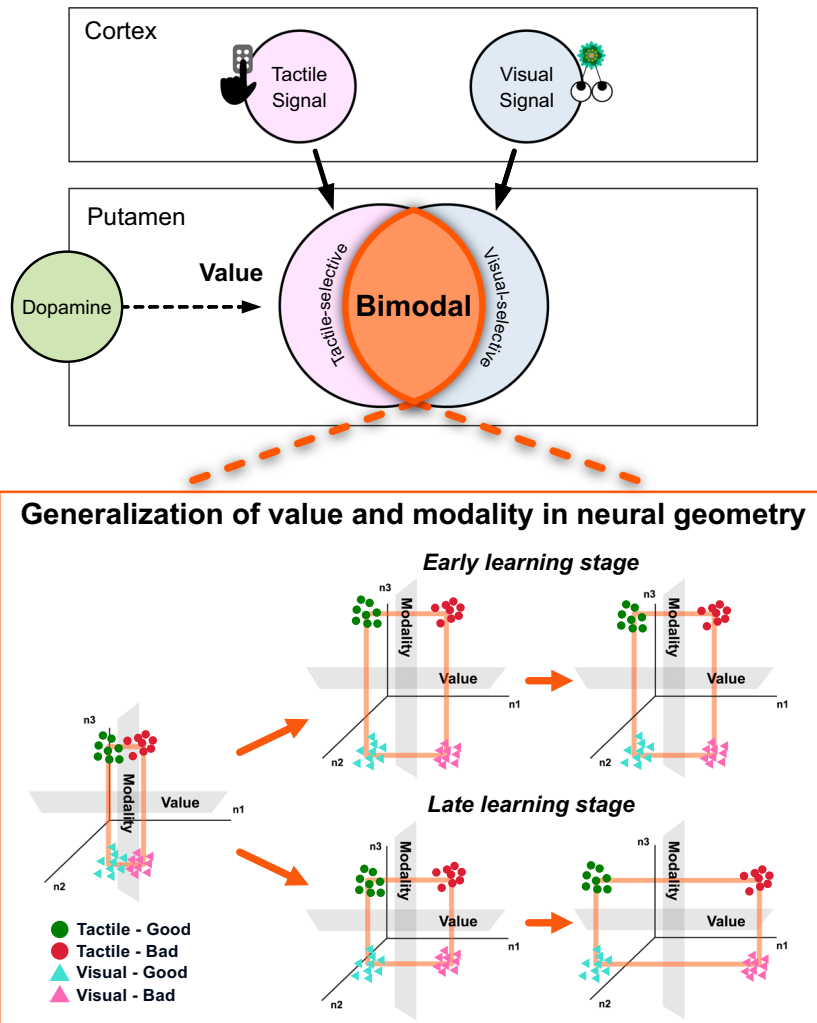


Fig. 8 | Efficient neural geometry of value and modality in the primate putamen reflects learning states. The neural geometry of bimodal value neurons representing value and modality evolves across learning and reflects value-guided behavior.

with a cognitive state reflecting well-adapted and well-learned value-guided behavior (Fig. 8). In contrast, this relationship between the neural geometry and behavioral outcomes was absent in modality-selective value neurons, indicating the unique role of bimodal value neurons in encoding the cognitive states underlying value-guided behavior.

Low-dimensional representation for efficient processing in the basal ganglia

It is noteworthy that putamen neurons process value and modality information using low-dimensional representations, a characteristic mostly reported in higher-order structures, such as the prefrontal cortex and hippocampus^{10,13,41,42}. This raises another question: Do

putamen neurons need to encode information in low-dimensional, generalized representations across shared modality or value features?

An important consideration is that the number of neurons decreases progressively from the putamen to subsequent structures^{43,44}. Within this anatomical funneling structure, reducing neural population patterns through shared representations may enable these downstream regions to process a diverse range of information efficiently with fewer neurons. Therefore, to convey information to subsequent structures without losses and to ensure proper processing in these downstream regions, the putamen may need to represent and transmit both value and modality information in a low-dimensional generalized form.

Additionally, considering energy consumption at the neuron level, generating a greater number of neural patterns requires more

energy because transitions between brain states necessitate synaptic changes, such as alterations in ion channel responses and structural modifications in the synapses, all of which demand an ATP supply⁹. Instead of requiring every neuron to examine every detail of individual pieces of information, processing based on shared features may offer potential efficiency gains by reducing the energy required for state changes. Therefore, the shared representation of putamen neurons enables the efficient processing of information with less energy.

Based on the shared representation found in putamen neurons, we also consider the possibility that downstream structures of the putamen, such as the substantia nigra pars reticulata and the globus pallidus internal segment, may process information using lower-dimensional representations. This is particularly linked to the question of how individual neurons' responses and population representations within each region are read out in subsequent regions of the basal ganglia system. Understanding how single-cell properties impact population representation and how neural population patterns contribute to actual brain functions remains a complex challenge in neuroscience^{35,41,45–50}. Additionally, whether different populations of neurons perform distinct functions remains an ongoing question^{27,51–53}. Future research will be crucial in uncovering how different structures within the basal ganglia encode various types of value-related information through low-dimensional, generalized representations. This will provide insight into the circuit-level mechanisms underlying value-guided behavior and how the entire basal ganglia network efficiently processes value and modality information.

Transformation of the neural geometry toward value abstraction reflects the adaptive state and learning stages of value-guided behavior

Recent studies have discussed the significance and advantages of abstract representation^{42,50,54}. One fundamental question is whether this representation correlates with behavior. Our findings show that the dynamic transformation of the neural geometry in the putamen shifts toward a more shared-value representation within a trial, suggesting its possible role in value-guided finger-insertion movements. Notably, as object-value reversal learning progressed, the neural geometry transformation accelerated, with a faster shift toward a shared-value representation during the late learning stage compared to the early stage. Additionally, this shift occurred more rapidly in adaptive trials than in unadaptive trials, suggesting that these dynamic changes are involved in value-guided movements.

This shift toward a shared-value representation also suggests that putamen neurons may be involved in the processing of the sensory-to-value transformation to guide goal-directed behavior. In our tasks, after experiencing a value-associated tactile or visual stimulus, distinguishing between good and bad values is essential for achieving the goal (a liquid reward). Because the final movement in both the T-VRT and V-VRT is the execution of a finger insertion guided by the perceived value, a clear recognition of good or bad values is sufficient to guide finger movements at the end of the trial. In this context, modality information may become irrelevant for value-guided movement once values are recognized. Therefore, the degree of value abstraction could be more directly associated with behavioral performance, with higher abstraction facilitating more effective action selection and execution to attain the goal. Our data suggest that successfully executing the final goal-directed action depends on the convergence of value meanings—across modalities—into a single, abstract representation of value, uninfluenced by other irrelevant sensory information.

In natural conditions, however, stimuli from different modalities, each associated with distinct values, are often presented simultaneously, necessitating the selection of the most valuable object among them. This suggests that the process of value encoding and abstraction may contribute differently under varying conditions. For example, a

previous study showed that neurons in the orbitofrontal cortex did not concurrently encode different values when stimuli were presented serially⁵⁵. In this study, we examined tactile and visual value separately in the putamen using two task paradigms designed to focus on values rather than sensory modalities. Thus, although we found that the neural geometry shifts toward a shared representation of crucial information and correlates with behavioral performance, it remains an open question as to how bimodal value neurons encode tactile and visual values when presented together. Additionally, it is yet to be determined whether they exhibit distinct dynamics in neural geometry when modality information plays a crucial role in achieving a goal.

Insight from dynamic neural geometry and conventional decoding in the putamen

The performance of value-guided behavior tends to correlate more strongly with the changing patterns of neural geometry than with the predictions obtained from the conventional decoding method. This occurs because the decoding accuracy rates for value and modality consistently exceeded 90% during phases 2 and 3 across the learning stages and adaptive states. These findings indicate that the transformation of the neural geometry into a shared-value representation is more sensitive during the capturing of a cognitive state in which putamen neurons encode the generalized reward expectancy for value-guided movements.

In contrast, these neurons did not exhibit a dynamic shift toward a shared modality representation; instead, they displayed more distinct representations for modality discrimination. However, our block-wise design of T-VRT and V-VRT should be considered, as it may convey not only modality information but also additional contextual cues. In this regard, the modality we refer to in this study is better understood as contextual modality rather than purely sensory modality. If monkeys can be successfully trained to learn an interleaved presentation of tactile and visual stimuli within a single block, it could provide further insight into whether putamen neurons specifically process sensory modality information.

Task difficulty should also be considered, as differences in difficulty between tasks may be embedded in the contextual information. We observed a higher give-up rate in V-VRT compared to T-VRT, while the reaction times to good stimuli were faster in T-VRT than V-VRT, demonstrating the challenge of directly comparing task difficulty levels. Nonetheless, the monkeys demonstrated a high level of proficiency, as their choice behavior during the task exceeded 94%, indicating that they were well trained in both T-VRT and V-VRT.

The correlation between the dynamic shift toward abstract value representation and behavioral performance underscores its potential for predicting value-guided behavior. Nonetheless, our reliance on pseudo-populations may have led to certain limitations as we attempted to fully capture the dynamics of neural information processing. Specifically, pseudo-populations do not account for trial-to-trial noise correlations, potentially leading to an overestimation of encoded information⁵⁶. Future advancements in simultaneous recording techniques for deep brain regions in primates could overcome these limitations. Additionally, our decoding used linear SVMs, which are interpretable but may miss nonlinear patterns, especially in complex interactions like value and modality⁵⁷. Future use of nonlinear methods may reveal additional structure in neural population activity. Such progress would enable the use of a dynamic shift toward shared-value representation to decode trial-by-trial cognitive states, improving our understanding of the neural mechanisms behind value-guided behavior.

Methods

General experimental procedures and subjects for electrophysiology

All of the data were collected in our previous study and were reanalyzed for the purposes of this study⁸. All experimental and animal care

procedures were approved by the Seoul National University Institutional Animal Care and Use Committee.

Two rhesus macaques (*Macaca mulatta*; female monkey EV (5.2 kg) and male monkey UL (10.7 kg)) were used for the experiments. During the period of general anesthesia and surgical preparation, the monkeys' skulls underwent implantation of a plastic head holder and a recording chamber. Each chamber was positioned at a lateral tilt of 25° to align with the putamen. Training and recording sessions commenced once the monkeys had completely recuperated from the surgery.

Single-unit recording

During the task performance by the monkey, the activities of individual neurons within the putamen were recorded using standard procedures. Determination of recording sites utilized a grid system with a spacing of 1 mm, aided by MR images (3T, Siemens) aligned with the chamber's direction. Single-unit recording employed a glass-coated electrode (Alpha-Omega) inserted into the brain through a stainless-steel guide tube and advanced using an oil-driven micromanipulator (MO-974A, Narishige). Neuronal signals were amplified, filtered (250 Hz to 10 kHz), and digitized (30-kHz sampling rate, 16-bit A/D resolution) using a Scout system (Ripple Neuro, UT). Online isolation of neuronal spikes was achieved through custom voltage-time window discrimination software (BLIP, Laboratory of Sensorimotor Research, National Eye Institute National Institutes of Health [LSR/NEI/NIH], accessible at www.cocila.net/blip), with corresponding timings detected at 1 kHz. Individual spike waveforms were recorded at 50 kHz. In addition, to verify the online isolation quality of putative single units when neuronal signals appeared to be mixed, we used online cross-correlation analysis using the BLIP software.

Behavioral tasks

Monkeys performed two different modality value tasks, termed here as the Tactile Value Reversal Task (T-VRT) and the Visual Value Reversal Task (V-VRT), as previously described⁸.

In the T-VRT task, monkeys were trained to insert their left index finger into the left hole of a braille presentation case upon being presented with a colored square cue on a screen. Once they inserted their fingers into the hole, a braille pattern was delivered and remained present for 500 milliseconds (ms). The monkeys were then instructed to maintain contact with the tactile stimulus until the disappearance of the finger-in cue and the tactile stimulus. Because the braille pattern was presented within an invisible braille case, the monkeys relied solely on tactile perception to discriminate its value. After retracting their finger from the hole, there was a delay period ranging randomly from 500 to 1000 ms. Subsequently, upon the onset of the second cue, the monkeys could either reinsert to touch the same stimulus that they had experienced before and receive a stimulus-associated reward, or give up reinserting their finger by waiting 1000 or 2000 ms. If they chose to reinsert the finger, they were required to maintain finger insertion for a minimum of 200 ms to receive the stimulus-associated reward. If they chose to give up the reinsertion, they would simply have to wait for the next trial.

The reaction time for finger insertion was measured from the onset of the second 'finger-in' cue to the actual finger insertion. Across two blocks, each consisting of 40–50 trials, the association between the stimulus and its value was reversed. Initially, in the first block, one stimulus was linked to a liquid reward, while the other was not. Subsequently, in the second block, this contingency was reversed. The order of the blocks was randomized across sessions, ensuring that the pairing of stimuli with rewards remained unknown to both the monkeys and the experimenters until the beginning of each session.

The procedure for V-VRT was identical to that of T-VRT, except that visual stimuli were presented instead of tactile stimuli. Reward-associated fractal images were displayed on a monitor screen when the

monkeys inserted their left index finger in response to the presentation of a cue. Fractal images were generated using a MATLAB-based program (<https://github.com/ProfKimHF/fractalgenerator>). The two modality tasks were conducted separately.

Single neuron categorization

We initially categorized neurons exhibiting task-related responses. Evaluating the task-related neuronal responses involved isolating the activity of individual neurons and calculating the spike counts during the T-VRT and V-VRT. For this assessment, we compared spike rates between the targeted test windows and control windows. Control windows were defined as the period 200–0 ms preceding the onset of the first finger-in cue, while test windows spanned 0–500 ms following the onset of each task event. Task events included (1) the first finger-in cue-on, (2) the first finger-in, (3) stimulus-on, (4) stimulus-off, (5) the first finger-out, (6) the second finger-in cue-on, (7) the second finger-in, (8) reward, (9) the second finger-in cue-off, and (10) the second finger-out. Statistical significance in task-related responses was determined by comparing spike counts between control and test windows in individual trials using the Wilcoxon rank-sum test. Neurons showing statistical significance in any of the tested task events were classified as task-related response neurons.

Among the neurons with task-related responses, we examined whether each neuron exhibited value discrimination responses during either the stimulus presentation in the first cue period or the delay period as previously described⁸. We quantified the activity of each individual neuron in response to tactile or visual stimuli by calculating the spike counts within a specified test window (0–500 ms after stimulus onset or the first finger-out) across individual trials. The firing rates of individual putamen neurons in response to good and bad values were compared using the Wilcoxon rank-sum test to determine the statistical significance of value discrimination. Subsequently, we analyzed the neural responses in both the T-VRT and V-VRT. Neurons displaying distinct value discrimination responses exclusively during either of the two T-VRT periods but not in the V-VRT period were categorized as 'tactile-selective value neurons'. Conversely, those demonstrating value discrimination responses solely during the V-VRT but not during the T-VRT were identified as 'visual-selective value-coding neurons'. Neurons exhibiting value discrimination responses in both the T-VRT and V-VRT were classified as 'bimodal value neurons'. Details pertaining to the definition of each type of value-coding neuron and the corresponding numbers are summarized in Supplementary Table S1.

Population decoding

We conducted pre-processing steps for population decoding. First, given our finding that the putamen encodes value responses in two distinct time phases - the stimulus presentation and blank delay period - we computed the spike train in both the stimulus presentation and the delay period. For the stimulus presentation period, we used a [−200, 500] ms window aligned with the stimulus onset, while for the delay period, a window [0, 500] ms aligned with the finger-out action was used.

Subsequently, these spike trains from the two periods were concatenated. We did not simply set the time window from [−200, 1000] ms from stimulus onset because doing so would encompass a finger-out movement between the stimulus being turned off and the start of the delay. As this study primarily focuses on value processing, we aimed to minimize neural responses caused by movements as much as possible by combining these two distinct time periods. Second, different analytic windows were used for either time-resolved decoding or fixed-window decoding methods. The time-resolved decoding depicted in Figs. 2B, 3B was done on spike counts measured in a 100-ms moving window with a 1-ms step size. For fixed-window decoding, we summed spike counts in a fixed window corresponding to each

time phase, as shown in Figs. 3–6. We reported averaged decoding accuracy rates across iteration results and used these values as the main dataset for the analysis and visualization. Concatenated spike trains were then normalized using the z-score to capture response changes across all neurons, as opposed to focusing solely on those with high firing rates.

Using these pre-processed activities of each neuron, we created pseudo-population data. Trials from each neuron were randomly selected, after which we utilized ten-fold cross-validation with a linear support vector machine (SVM) decoder to evaluate the performance. This procedure was repeated for 100 resample runs, where different random pseudo-populations were created during each run. We presented decoding results for three task variables: 1) modality, 2) value, and 3) interaction between modality and value. We ensured that an equal number of trials per condition (for interaction between modality and value, tactile-good, tactile-bad, visual-good, and visual-bad) were contributed by each cell included in the population decoding step. For all analyses, data were aggregated across monkeys, given that all key features of the dataset remained consistent between the two monkeys.

Permutation model to test the decoding performance for significance

A permutation test was conducted by shuffling the labels of each trial condition in each neuron. The same decoding procedure was used to generate a null distribution of the decoding accuracy rates. This procedure was repeated 1000 times and generated a full shuffled decoding null distribution for each time bin. We reported the theoretical chance level for each tested condition in the main figures and the fifth to the ninety-fifth percentiles of the null distribution in the Supplementary Figures. The *p*-value was calculated through a right-tailed z-test by comparing the decoder's performance with the null distribution. If the *p*-value was below 0.05, we defined the decoder's performance as significantly higher than the permutation results. The raw *p*-values from this analysis are subject to multiple comparison issues, as the analysis was conducted across multiple time points^{17,27}. To address this, we applied false discovery rate (FDR) correction using the Benjamini–Hochberg procedure to control for the proportion of false positives. In addition, in order to maintain a conservative approach in our analysis when using time-resolved windows, we tabulated consecutive significant points and reported significance only when at least 20 consecutive time points displayed significance.

Dimensionality reduction

Dimensionality reduction was employed to represent the decoding outcomes and the structure of population neural patterns visually. This was achieved by conducting a principal component analysis (PCA) of the averaged z-scored neural activities per condition. PCA was applied to a firing rate matrix with dimensions of $CT \times N$, where *C* represents the number of conditions, *T* denotes the number of time points per condition, and *N* indicates the number of neurons. With the exception of Fig. 2D, which depicts neural trajectories with time-resolved activities, we analyzed and visualized all neural data across both monkeys.

Cross-condition generalization performance (CCGP)

To quantify the extent of generalization across shared conditions and the geometry of neural activities at the population level, we assessed the CCGP in our experiment¹⁰. Unlike the traditional cross-validated decoding (support vector machine (SVM)), where trials from all conditions are present in both the training and test sets, the CCGP used trials from distinct conditions for the training and test sets. For instance, when testing for 'value', we could designate the conditions 'tactile good' and 'tactile bad' as the 'good' and 'bad' conditions for training a decoder (Fig. 3A). Subsequently, we assessed whether the trained decoder could accurately classify the conditions 'visual good'

and 'visual bad' as 'good' and 'bad', respectively. By evaluating the classification performance on data from entirely different conditions, we could assess the similarity of population neural patterns among distinct conditions with shared variables and the decoder's ability to generalize to novel conditions on which it has not been trained previously.

As we used a total of four conditions (tactile good, tactile bad, visual good, and visual bad), there are four possible combinations available to select training and testing sets for each variable (modality and value). Similar to population decoding, we assessed the CCGP on 100 iterations for each possible combination and averaged the results across iterations. Subsequently, we averaged the CCGP outcomes across all four combinations and reported these values as the main dataset.

Geometric random model to test the significance of the CCGP

To assess the significance of the CCGP, we followed the geometric random model used by Bernardi and colleagues¹⁰. This model involved creating a random geometry by relocating a cluster of points corresponding to different conditions to new random positions sampled from an isotropic Gaussian distribution. Subsequently, we rescaled all of the vectors to maintain the total variance across all conditions, known as the signal variance or variance of the centroids of the clusters. These procedures allowed us to evaluate the geometry of neural patterns for each condition in a more conservative manner as compared to the normal random labeling technique used in traditional population decoding.

For each possible CCGP combination, we conducted 1000 iterations and averaged the results across combinations. Based on these averaged results for each time point, we generated a null model and tested the significance of the CCGP. This rigorous approach enabled us to accurately evaluate the significance of our findings regarding the geometry of neural patterns across different conditions. A right-tailed z-test was conducted to test the CCGP outcomes for statistical significance.

Rationale behind dividing three fixed time phases

To examine the dynamic changes in geometries for generalized representation comprehensively, we segmented neural activities into three distinct, non-overlapping phases. Phase 1 comprises prestimulus-early stimulus periods (200 ms before and 150 ms after stimulus onset) to analyze neural pattern transitions before and after stimulus presentation. Phase 2, ranging from 150 ms to 500 ms after stimulus onset, captures the stimulus presentation period before the onset of the delay period. Phase 3 covers the entire blank delay period. These intervals were strategically chosen to optimize the visualization and analysis of the neural representation geometry. We analyzed the phase 2 starting at 150 ms after stimulus presentation because previous research by Merchant et al.⁵⁸ demonstrated that putamen neurons begin processing tactile stimuli within the range of 100–200 ms following stimulus onset. Furthermore, our investigation into the latency of value discrimination responses among bimodal value neurons during stimulus presentation in both the T-VRT and V-VRT tasks revealed median latencies of 141 ms for the T-VRT and 130 ms for the V-VRT⁸. These findings suggest that the critical period for stimulus-related information processing in the putamen occurs at around 150 ms, thereby informing our phase partitioning strategy for the analysis.

Parallelism score (PS) and corresponding permutation test

To measure the geometry of neural representations more precisely, we estimated the parallelism score (PS)¹⁰. To estimate the coding direction between two conditions, we trained a linear support vector machine (SVM) and used the resulting weight vector as a proxy for the axis separating the two classes in firing rate space. In our experiment, each

variable had only two coding directions from the two pairs of training conditions. We normalized the two weight vectors and computed the cosine of the angle between them. For example, to calculate the PS for value, we initially trained two linear classifiers, one with [tactile good, tactile bad] and the other with [visual good, visual bad]. Then, we computed the two coding vectors from each of these classifiers and calculated the cosine angle between them. This process was repeated 100 times, and the average PS for each condition was reported.

To test the statistical significance of the PS, we generated 1000 numbers for the null model with random labeling and calculated the cosine angle of the weight vectors for a comparison with the normal PS. A two-tailed z-test was conducted to test the PS for statistical significance.

Categorization of stimulus and delay value neurons

To examine whether stronger value encoding in a specific phase leads to differences in population representation, we used standards identical to those in our previous study. Bimodal value neurons were categorized into two types. For each neuron, we quantified the magnitude of value discrimination using receiver operating characteristic (ROC) analysis, which assessed how well the firing rates differentiated between good and bad values. ROC values were computed within two predefined time windows, the stimulus and delay periods, based on spike counts in each condition. Neurons were categorized based on their responses in each period using a ROC curve calculated with the activities of individual neurons to good stimuli versus bad stimuli. If a neuron showed stronger value responses ($|ROC - 0.5|$) during the stimulus presentation period than during the delay period, we identified it as a stimulus value neuron. In the opposite case, neurons were classified as delay value neurons.

Data analysis tool and statistics

All behavioral and neuronal data analyses were performed using MATLAB (R2023b). A summary of all statistical tests employed in this study is provided in Supplementary Table 2.

Reporting summary

Further information on research design is available in the Nature Portfolio Reporting Summary linked to this article.

Data availability

Due to ethical and regulatory restrictions, the dataset supporting this study cannot be publicly archived. Access to the data requires prior approval from the Institutional Animal Care and Use Committee of Seoul National University and National Research Foundation of Korea. Requests will be reviewed within several months and, if approved, data will be made available for academic, non-commercial use. Source data are provided with this paper.

Code availability

Custom code associated with this study is available at <https://github.com/ProfKimHF>.

References

- Bergman, H. et al. Physiological aspects of information processing in the basal ganglia of normal and parkinsonian primates. *Trends Neurosci.* **21**, 32–38 (1998).
- Alexander, G. E. & Crutcher, M. D. Functional architecture of basal ganglia circuits: neural substrates of parallel processing. *Trends Neurosci.* **13**, 266–271 (1990).
- Nambu, A. Somatotopic organization of the primate basal ganglia. *Front. Neuroanat.* **5**, 1–9 (2011).
- Flaherty, A. W. & Graybiel, A. M. Corticostriatal transformations in the primate somatosensory system. Projections from physiologically mapped body-part representations. *J. Neurophysiol.* **66**, 1249–1263 (1991).
- Alexander, G. E., DeLong, M. R. & Strick, P. L. Parallel organization of functionally segregated circuits linking basal ganglia and cortex. *Annu. Rev. Neurosci.* **9**, 357–381 (1986).
- Bar-Gad, I., Morris, G. & Bergman, H. Information processing, dimensionality reduction and reinforcement learning in the basal ganglia. *Prog. Neurobiol.* **71**, 439–473 (2003).
- Percheron, G. & Fillion, M. Parallel processing in the basal ganglia: up to a point. *Trends Neurosci.* **14**, 55–59 (1991).
- Hwang, S.-H., Park, D., Lee, J.-W., Lee, S.-H. & Kim, H. F. Convergent representation of values from tactile and visual inputs for efficient goal-directed behavior in the primate putamen. *Nat. Commun.* **15**, 8954 (2024).
- Harris, J. J., Jolivet, R. & Attwell, D. Synaptic energy use and supply. *Neuron* **75**, 762–777 (2012).
- Bernardi, S. et al. The geometry of abstraction in the hippocampus and prefrontal cortex. *Cell* **183**, 954–967.e21 (2020).
- Boyle, L. M., Posani, L., Irfan, S., Siegelbaum, S. A. & Fusi, S. Tuned geometries of hippocampal representations meet the computational demands of social memory. *Neuron* **112**, 1358–1371.e9 (2024).
- Chien, J. M., Wallis, J. D. & Rich, E. L. Abstraction of reward context facilitates relative reward coding in neural populations of the macaque anterior cingulate cortex. *J. Neurosci.* **43**, 5944–5962 (2023).
- Nogueira, R., Rodgers, C. C., Bruno, R. M. & Fusi, S. The geometry of cortical representations of touch in rodents. *Nat. Neurosci.* **26**, 239–250 (2023).
- Fascianelli, V. et al. Neural representational geometries reflect behavioral differences in monkeys and recurrent neural networks. *Nat. Commun.* **15**, 6479 (2024).
- Wójcik, M. J. et al. Learning shapes neural geometry in the prefrontal cortex. *bioRxiv* <https://doi.org/10.1101/2023.04.24.538054> (2023).
- Crutcher, M. D. & DeLong, M. R. Single cell studies of the primate putamen. *Exp. Brain Res.* **53**, 233–243 (1984).
- Seo, M., Lee, E. & Averbach, B. B. Action selection and action value in frontal-striatal circuits. *Neuron* **74**, 947–960 (2012).
- Kimura, M. Behaviorally contingent property of movement-related activity of the primate putamen. *J. Neurophysiol.* **63**, 1277–1296 (1990).
- Alexander, G. E. Selective neuronal discharge in monkey putamen reflects intended direction of planned limb movements. *Exp. Brain Res.* **67**, 623–634 (1987).
- Kang, J. et al. Primate ventral striatum maintains neural representations of the value of previously rewarded objects for habitual seeking. *Nat. Commun.* **12**, 1–13 (2021).
- Kim, H. F. & Hikosaka, O. Distinct basal ganglia circuits controlling behaviors guided by flexible and stable values. *Neuron* **79**, 1001–1010 (2013).
- Van Hoesen, G. W., Yeterian, E. H. & Lavizzo-Mourey, R. Widespread corticostriate projections from temporal cortex of the rhesus monkey. *J. Comp. Neurol.* **199**, 205–219 (1981).
- Künzle, H. Projections from the primary somatosensory cortex to basal ganglia and thalamus in the monkey. *Exp. Brain Res.* **30**, 481–492 (1977).
- Flaherty, A. W. & Graybiel, A. M. Input-output organization of the sensorimotor striatum in the squirrel monkey. *J. Neurosci. J. Soc. Neurosci.* **14**, 599–610 (1994).
- Hori, Y., Minamimoto, T. & Kimura, M. Neuronal encoding of reward value and direction of actions in the primate putamen. *J. Neurophysiol.* **102**, 3530–3543 (2009).
- Muranishi, M. et al. Inactivation of the putamen selectively impairs reward history-based action selection. *Exp. Brain Res.* **209**, 235–246 (2011).

27. An, S., Hwang, S.-H., Lee, K. & Kim, H. F. The primate putamen processes cognitive flexibility alongside the caudate and ventral striatum with similar speeds of updating values. *Prog. Neurobiol.* **243**, 102651 (2024).
28. Kunimatsu, J., Maeda, K. & Hikosaka, O. The caudal part of putamen represents the historical object value information. *J. Neurosci.* **39**, 1709–1719 (2019).
29. Cohen, Y., Schneidman, E. & Paz, R. The geometry of neuronal representations during rule learning reveals complementary roles of cingulate cortex and putamen. *Neuron* **109**, 839–851.e9 (2021).
30. Slezee, B. J. & Hayden, B. Y. Differential contributions of ventral and dorsal striatum to early and late phases of cognitive set reconfiguration. *J. Cogn. Neurosci.* **28**, 1849–1864 (2016).
31. Jackson, S. A. W. et al. Selective role of the putamen in serial reversal learning in the marmoset. *Cereb. Cortex* **29**, 447–460 (2019).
32. Nambu, A., Kaneda, K., Tokuno, H. & Takada, M. Organization of corticostriatal motor inputs in monkey putamen. *J. Neurophysiol.* **88**, 1830–1842 (2002).
33. Crutcher, M. D. & DeLong, M. R. Single cell studies of the primate putamen. I. Functional organization. *Exp. Brain Res.* **53**, 233–243 (1984).
34. Buonomano, D. V. & Maass, W. State-dependent computations: spatiotemporal processing in cortical networks. *Nat. Rev. Neurosci.* **10**, 113–125 (2009).
35. Churchland, M. M. et al. Neural population dynamics during reaching. *Nature* **487**, 51–56 (2012).
36. Remington, E. D., Narain, D., Hosseini, E. A. & Jazayeri, M. Flexible sensorimotor computations through rapid reconfiguration of cortical dynamics. *Neuron* **98**, 1005–1019.e5 (2018).
37. Mante, V., Sussillo, D., Shenoy, K. V. & Newsome, W. T. Context-dependent computation by recurrent dynamics in prefrontal cortex. *Nature* **503**, 78–84 (2013).
38. Johnston, W. J. & Fusi, S. Abstract representations emerge naturally in neural networks trained to perform multiple tasks. *Nat. Commun.* **14**, 1–18 (2023).
39. Peysakhovich, B. et al. Primate superior colliculus is causally engaged in abstract higher-order cognition. *Nat. Neurosci.* **27**, 1999–2008 (2024).
40. Miyachi, S., Hikosaka, O., Miyashita, K., Kárádi, Z. & Rand, M. K. Differential roles of monkey striatum in learning of sequential hand movement. *Exp. Brain Res.* **115**, 1–5 (1997).
41. Rigotti, M. et al. The importance of mixed selectivity in complex cognitive tasks. *Nature* **497**, 585–590 (2013).
42. She, L., Benna, M. K., Shi, Y., Fusi, S. & Tsao, D. Y. Temporal multiplexing of perception and memory codes in IT cortex. *Nature* **629**, 861–868 (2024).
43. Oorschot, D. E. Total number of neurons in the neostriatal, pallidal, subthalamic, and substantia nigral nuclei of the rat basal ganglia: a stereological study using the cavalieri and optical disector methods. *J. Comp. Neurol.* **366**, 580–599 (1996).
44. Lanciego, J. L., Luquin, N. & Obeso, J. A. Functional neuroanatomy of the basal ganglia. *Cold Spring Harb. Perspect. Med.* **2**, a009621 (2012).
45. Saxena, S. & Cunningham, J. P. Towards the neural population doctrine. *Curr. Opin. Neurobiol.* **55**, 103–111 (2019).
46. Câteau, H. & Reyes, A. D. Relation between single neuron and population spiking statistics and effects on network activity. *Phys. Rev. Lett.* **96**, 58101 (2006).
47. Crumiller, M., Knight, B. & Kaplan, E. The measurement of information transmitted by a neural population: promises and challenges. *Entropy* **15**, 3507–3527 (2013).
48. Johnston, W. J., Palmer, S. E. & Freedman, D. J. Nonlinear mixed selectivity supports reliable neural computation. *PLoS Comput. Biol.* **16**, 1–37 (2020).
49. Barak, O., Rigotti, M. & Fusi, S. The sparseness of mixed selectivity neurons controls the generalization-discrimination trade-off. *J. Neurosci.* **33**, 3844–3856 (2013).
50. Ostojic, S. & Fusi, S. Computational role of structure in neural activity and connectivity. *Trends Cogn. Sci.* **28**, 677–690 (2024).
51. Fine, J. M. et al. Abstract value encoding in neural populations but not single neurons. *J. Neurosci.* **43**, 4650–4663 (2023).
52. Biglari, N. et al. Functionally distinct POMC-expressing neuron subpopulations in hypothalamus revealed by intersectional targeting. *Nat. Neurosci.* **24**, 913–929 (2021).
53. Jiang, X., Saggar, H., Ryu, S. I., Shenoy, K. V. & Kao, J. C. Structure in neural activity during observed and executed movements is shared at the neural population level, not in single neurons. *Cell Rep.* **32**, 108006 (2020).
54. Kriegeskorte, N. & Kievit, R. A. Representational geometry: integrating cognition, computation, and the brain. *Trends Cogn. Sci.* **17**, 401–412 (2013).
55. Ferro, D., Cash-Padgett, T., Wang, M. Z., Hayden, B. Y. & Moreno-Bote, R. Gaze-centered gating, reactivation, and reevaluation of economic value in orbitofrontal cortex. *Nat. Commun.* **15**, 6163 (2024).
56. Moreno-Bote, R. et al. Information-limiting correlations. *Nat. Neurosci.* **17**, 1410–1417 (2014).
57. Fortunato, C. et al. Nonlinear manifolds underlie neural population activity during behaviour. *bioRxiv Prepr. Serv. Biol.* <https://www.biorxiv.org/content/10.1101/2023.07.18.549575v3> (2024).
58. Merchant, H., Zainos, A., Hernández, A., Salinas, E. & Romo, R. Functional properties of primate putamen neurons during the categorization of tactile stimuli. *J. Neurophysiol.* **77**, 1132–1154 (1997).

Acknowledgements

This work was supported by the Basic Science Research Program (RS-2024-00339355), ASTRA Program (RS-2024-00436783), Bio&Medical Technology Development Program (RS-2025-02263832), and Global-LAMP Program (RS-2023-00301976) through the National Research Foundation (NRF) of Korea.

Author contributions

H.F.K. supervised the entire project. S.H.H. and J.W.L. performed the behavior and single-unit recording experiments. S.H.H., J.W.L., S.P.K. and H.F.K. analyzed the data and prepared the figures. S.H.H., J.W.L. and H.F.K. wrote the first draft, and S.H.H., J.W.L., S.P.K. and H.F.K. interpreted data and wrote the final manuscript.

Competing interests

The authors declare no competing interests.

Additional information

Supplementary information The online version contains supplementary material available at <https://doi.org/10.1038/s41467-025-63822-3>.

Correspondence and requests for materials should be addressed to Hyoung F. Kim.

Peer review information *Nature Communications* thanks Cyriel Pennartz and the other, anonymous, reviewer(s) for their contribution to the peer review of this work. A peer review file is available.

Reprints and permissions information is available at <http://www.nature.com/reprints>

Publisher's note Springer Nature remains neutral with regard to jurisdictional claims in published maps and institutional affiliations.

Open Access This article is licensed under a Creative Commons Attribution-NonCommercial-NoDerivatives 4.0 International License, which permits any non-commercial use, sharing, distribution and reproduction in any medium or format, as long as you give appropriate credit to the original author(s) and the source, provide a link to the Creative Commons licence, and indicate if you modified the licensed material. You do not have permission under this licence to share adapted material derived from this article or parts of it. The images or other third party material in this article are included in the article's Creative Commons licence, unless indicated otherwise in a credit line to the material. If material is not included in the article's Creative Commons licence and your intended use is not permitted by statutory regulation or exceeds the permitted use, you will need to obtain permission directly from the copyright holder. To view a copy of this licence, visit <http://creativecommons.org/licenses/by-nc-nd/4.0/>.

© The Author(s) 2025